PUBLICATIONS OF THE ASTRONOMICAL SOCIETY OF THE PACIFIC, **126**:565–572, 2014 June

On-Sky Speckle Nulling Demonstration at Small Angular Separation with SCExAO

FRANTZ MARTINACHE,[1,2] OLIVIER GUYON,[1,3] NEMANJA JOVANOVIC,[1] CHRISTOPHE CLERGEON,[1]
GARIMA SINGH,[1] TOMOYUKI KUDO,[1] THAYNE CURRIE,[4] CHRISTIAN THALMANN,[5,6]
MICHAEL MCELWAIN,[7] AND MOTOHIDE TAMURA[8]

Received 2013 September 16; accepted 2014 May 04; published 2014 June 11

ABSTRACT. This paper presents the first on-sky demonstration of speckle nulling, which was achieved at the Subaru Telescope in the context of the Subaru Coronagraphic Extreme Adaptive Optics (SCExAO) Project. Despite the absence of a high-order high-bandwidth closed-loop AO system, observations conducted with SCExAO show that even in poor-to-moderate observing conditions, speckle nulling can be used to suppress static and slow speckles even in the presence of a brighter dynamic speckle halo, suggesting that more advanced high-contrast imaging algorithms developed in the laboratory can be applied to ground-based systems.

Online material: color figures

1. INTRODUCTION

The detection of high-contrast features such as disks and companions in diffraction-limited images relies for the most part on the characterization and calibration of diffraction effects, whether static (induced by the geometry of the pupil and the aberrations in the optics), quasi-static (telescope pointing and slowly variable instrument alignment), or dynamic (atmosphere-induced). For ground-based observations, the best performance comes from a combination of adaptive optics (AO), which address the dominant atmospheric term, turning the seeing-limited image into a diffraction-limited one, and post-processing techniques based on differential imaging. These include spectral, polarimetric or angular differential imaging (ADI), the first two relying upon some properties of the target, such as the presence of specific spectral features or a polarimetric signature.

ADI (Marois et al. 2006; Lafrenière et al. 2007) provides the means to calibrate the static and quasi-static features of the PSF by observing a target with an alt-azimuthal telescope, for which the sky rotates relative to the telescope pupil. If enough field rotation occurs over a time that is less than the characteristic quasi-static aberration time-scale, the diversity between the orientation of the sky and the quasi-static point spread function (PSF) allows the calibration of the diffraction pattern, leading to greatly enhanced detection limits.

The calibration requires that the angular rotation induces sufficient local linear displacement of the genuine features, such as faint companions, relative to the quasi-static PSF (Marois et al. 2006) in order to avoid self-subtraction. While highly efficient at angular separations greater than 1″, it is difficult to benefit from this technique at angular separations smaller than 0.5″. For addressing such small angular separations, two approaches are possible: interferometric calibration and additional active wavefront control.

Interferometric calibration of diffraction-limited images is a nascent field that inherits from the ideas and techniques of sparse aperture masking (SAM), a.k.a., nonredundant masking (NRM) interferometry with AO (Tuthill et al. 2006). The fundamental idea behind these techniques is that although the content of images may be corrupted by residual aberrations, it is possible to construct a subset of information that is independent from these aberrations. One possible such subset of information is the kernel-phase (Martinache 2010) which, just like sparse aperture masking using closure phase, goes as far as enabling the direct detection of high contrast features beyond the diffraction limit, a regime referred to as super-resolution (Pope et al. 2013). The fundamental advantage of this approach is that it requires no additional differential "trick" like ADI, although it is for now restricted to well-corrected AO images. Recent improvements of the technique, such as the statistically independent kernel-phase and better calibration procedures

[1] National Astronomical Observatory of Japan, Subaru Telescope, Hilo, HI 96720, frantz@naoj.org.
[2] Laboratoire Lagrange, UMR7293, Université de Nice Sophia-Antipolis, CNRS, Observatoire de la Côte d'Azur.
[3] Stewart Observatory, University of Arizona, Tucson, AZ 85721.
[4] Department of Astronomy and Astrophysics, University of Toronto, Canada.
[5] Astronomical Institute "Anton Pannekoek", University of Amsterdam, Science Park 904, 1098 XH Amsterdam, Netherlands.
[6] Department for Astronomy, ETH Zurich, CH-8093 Zurich, Switzerland.
[7] Goddard Space Flight Center, Greenbelt, MD.
[8] National Astronomical Observatory of Japan, 2-21-1 Osawa, Mitaka, Tokyo 181-8588, Japan.

described by Ireland (2013), show promise of performance that compares to what is currently achieved by ADI at small angular separations.

The alternative approach to the passive calibration by interferometry is to employ additional wavefront control to modulate the diffraction at small angular separation and create the diversity that enables the separation of genuine structure from diffraction features in the image. This concept, which can be referred to as coherence differential imaging (CDI), is very relevant to the upcoming generation of so called extreme AO (XAO) projects: Palm-3000/P1640 at Palomar (Oppenheimer et al. 2012), GPI at Gemini (Macintosh et al. 2008), SPHERE at VLT (Sauvage et al. 2010), and SCExAO at the Subaru Telescope (Martinache et al. 2011).

Among these projects, the Subaru Coronagraphic Extreme AO (SCExAO) project is unique with its incremental deployment schedule that enabled the on-sky testing of fundamental features of the instrument (Jovanovic et al., in preparation) prior to completion of its closed-loop XAO system (Clergeon et al. 2013). In this paper, we present the first convincing demonstration of on-sky closed-loop diffraction modulation, after an upstream AO correction is performed, providing a Strehl on the order of 20%. While the demonstrated gain is moderate and there is room for improvement, the paper nevertheless demonstrates that it is possible to control the features of a coronagraphic PSF near the inner working angle of the coronagraph using the speckle nulling approach introduced in previous work.

2. SCEXAO BEFORE XAO

What is usually referred to as an XAO system is a unit capable of producing a very stable and high-quality PSF, characterized by a Strehl ratio on the order of 90%. This very high level of Strehl, corresponding to residual wavefront errors on the order of $\lambda/20$ (where λ is the wavelength of observation), is indeed required for the high-contrast technique of coronagraphy, which aims to block the light of an on-axis bright source and reveal its circumstellar environment, in particular disk and/or faint companions.

Particularly in monochromatic light, it is possible to design coronagraphs that provide near-perfect extinction, and an inner working angle (IWA) that approaches the limit of diffraction (λ/D), where D represents the diameter of the telescope aperture. Examples of such coronagraphs include the vortex (Mawet et al. 2010) and the PIAA (Guyon 2003), both implemented on SCExAO. In practice, however, their performance is entirely dictated by the residual wavefront errors. Under poor Strehl conditions, the coronagraph does little more than allow the exposure time to be increased before saturation of the detector.

SCExAO does not currently support a high-order closed-loop AO system, expected to be first commissioned in 2014 fall. In this first phase of the project, SCExAO therefore relies entirely on the upstream Subaru Telescope facility AO system called AO188 (Minowa et al. 2010). AO188 and the coronagraphic imager HiCIAO (Hodapp et al. 2008) form the workhorse of the Strategic Exploration of Exoplanets and Disks with Subaru (SEEDS) observing campaign (Tamura 2009). SCExAO was conceived as a replacement upgrade for the current fore-optics used by HiCIAO, that should include a small IWA PIAA-based coronagraph as well as additional wavefront manipulation capability.

Therefore, while SCExAO does not currently qualify as an XAO system, it nevertheless already implements a 1-k actuator deformable mirror (DM). We have recently shown, using a calibration source in a stable laboratory environment, that the DM and the PIAA coronagraph used together can produce a high-contrast region in the field-of-view, with a 2.2 λ/D IWA (Martinache et al. 2012), with a simple iterative speckle-nulling loop. Using the same approach on-sky, relying on AO188 to produce a 20% Strehl ratio PSF, we demonstrate that it is possible to use speckle nulling to drive down the brightness of the diffraction features at small angular separation. We also show that the DM provides a flexible calibration tool that notably enables astrometric calibration as well as direct measurements of the contrast in images.

3. ON-SKY CORONAGRAPHIC CALIBRATION

Figure 1 provides a schematic overview of the optical layout of the near-IR arm of SCExAO, as it was used on the observing night of 2012 November 12. The upstream AO188 system feeds the instrument with a partially corrected $\mathrm{f}/14$ convergent beam, intercepted by a first tip-tilt controlled mirror located in an image plane and mounted on a focusing stage, and further steered by a second tip-tilt controlled mirror. This combination provides full control of the origin and incidence of the beam entering the coronagraph. The other important feature is the focal plane mask, reflecting the light of any on-axis source onto a camera used to sense the pointing, a subsystem called the coronagraphic low-order wavefront sensor (CLOWFS), as described by Guyon et al. (2009) and Vogt et al. (2011).

In addition, the system also comprises the PIAA remapping optics (Guyon et al. 2005) located before the focal plane mask and their inverse counterpart located after the focal plane mask. Recent work (Martinache et al. 2012) showed that when used together, the presence of these two sets of remapping optics can be ignored by the focal plane based wavefront control algorithm. Reflecting upon this conclusion, this discussion will ignore the remapping optics, which for the results presented in this paper, are always in the beam.

One of the two tip-tilt mirrors that steers the beam entering the coronagraph is the 1024-actuator DM itself which, while not exactly located in a pupil plane, can nevertheless be used to introduce/compensate for diffraction features in the coronagraphic image. The square grid geometry of the actuators underneath the DM membrane makes it particularly well-suited to generate

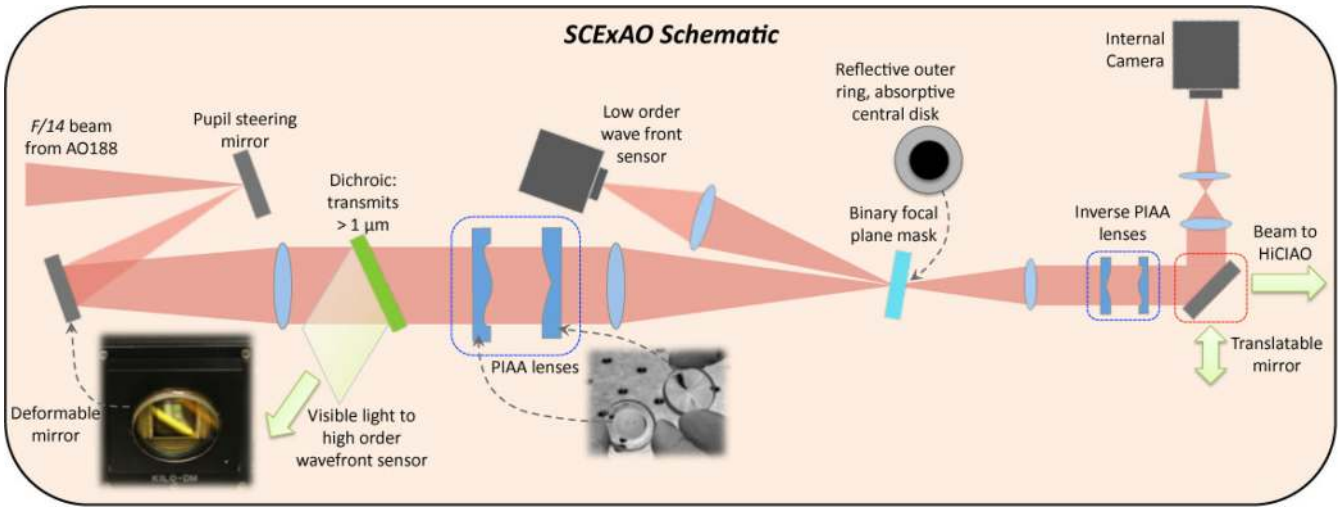

FIG. 1.—Schematic representation of the optics inside the SCExAO IR coronagraph used to produce the results presented in this paper. See the electronic edition of the *PASP* for a color version of this figure.

pairs of speckles that interfere with already present diffraction features in the coronagraphic image. The total number of actuators across the telescope pupil footprint imposes the size of the region of the coronagraphic image that can be probed by the DM, which will be referred to as the control region. As explained by Martinache et al. (2012), the control region with this current implementation fits within a $27.2 \times 24.8\ \lambda/D$ rectangular box. It is possible to generate a pair of speckles centered around the optical axis within this region by applying a sinusoidal displacement map on the DM.

Each such sinusoidal displacement map on the DM is characterized by four numbers: two cartesian coordinates of spatial frequency (k_x, k_y), one amplitude α (in radians) limited by the stroke of the DM, and a phase φ that can take any value between 0 and 2π. When applying a sinusoidal displacement map, the DM acts like a diffraction grating that creates off-axis copies of the on-axis bright source. Figure 2 illustrates the relation between DM modulation and speckles in the image. The larger the spatial frequency parameters, the faster the sinusoidal modulation of the DM surface and the further the corresponding pair of speckles lies away from the center of the control region. The larger the amplitude of the modulation, the brighter the resulting speckles. The phase does not change the intensity of the speckles unless they interfere with other coherent features in the image. Sinusoidal modulations of distinct properties can be added to the DM as long as the total requested range of displacement does not go beyond the DM stroke, creating in turn multiple pairs of speckles in the image.

The ability to produce symmetric pairs of speckles of controllable positions and contrast is a very convenient feature that facilitates otherwise difficult calibration procedures when observing with a coronagraph. Indeed, unlike classical imaging techniques and interferometric methods for which absolute control of the pointing is not a strict requirement (since the central star remains visible), the image of the star needs to be precisely driven and stabilized on the axis of the coronagraph for an efficient suppression.

Sivaramakrishnan & Oppenheimer (2006) astutely proposed to address this issue by inserting a reticulate grid of wires in the pupil plane that produces a predefined periodic diffraction pattern in the image. The grid geometry of deformable mirrors such as the 1k-actuator MEMS DM used in SCExAO can advantageously be used as an adaptive version of this reticulate grid. Just as described by Sivaramakrishnan & Oppenheimer (2006), the added satellite speckles provide a very reliable way to position the star behind the focal plane mask during target acqusition. Once in the ideal position, the low-order wavefront sensor (Guyon et al. 2009) keeps the image in a fixed position relative to the mask. During the post-processing stage, in case noncoherent structures such as companions are identified in the image, the satellite speckles offer a reliable astrometric reference.

In addition to offering astrometric and pointing aids (Hinkley et al. 2013), the generated speckles can be used for contrast calibration purposes. This can efficiently be achieved by an offline predetermination of the satellite speckle contrast relative to the central PSF as a function of spatial frequency and amplitude. Figure 3 shows one example of such on-sky contrast calibrated images, recorded by the coronagraphic imager HiCIAO fed light by SCExAO. The top panel of Figure 3 shows a nonsaturated low-exposure time image with the SCExAO focal plane mask out of the way. A sinusoidal modulation of the SCExAO DM of known characteristics creates a pair of speckles of controlled contrast. The bottom panel shows an image acquired with the same exposure time, this time with the SCExAO focal plane mask placed on-axis. Except at small angular separation, one can observe very little impact of the focal plane mask on the halo PSF features.

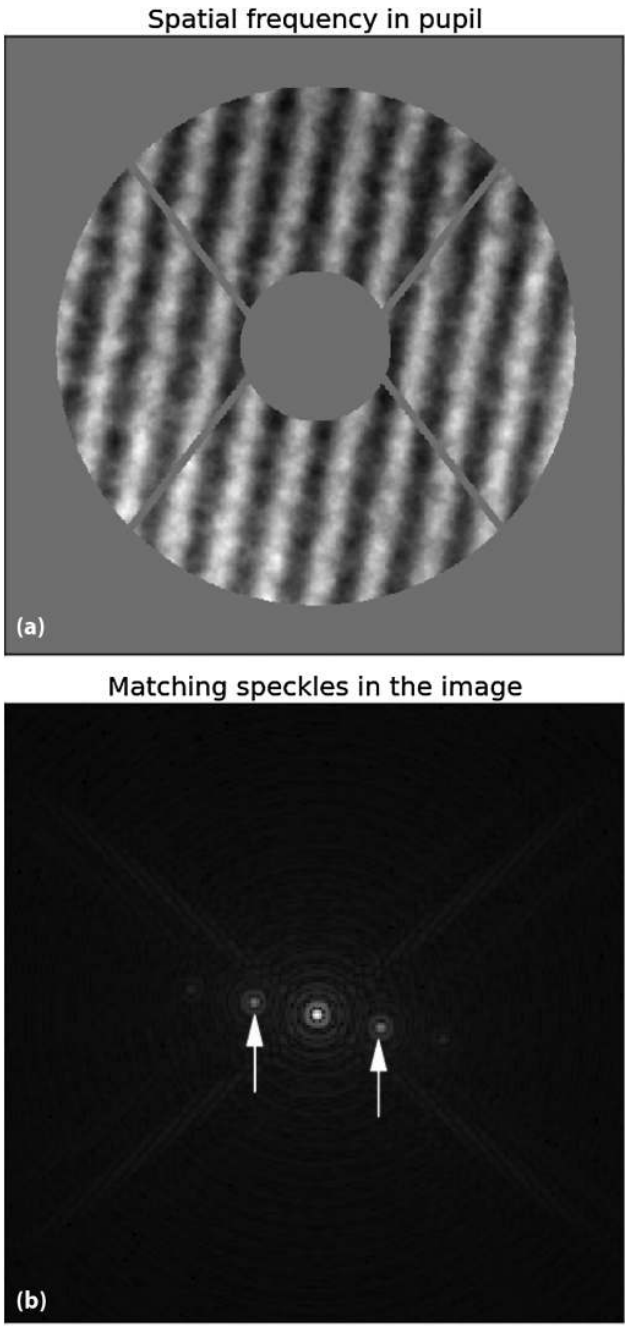

FIG. 2.—Illustration of the relation between sinusoidal modulation of the DM shape in the pupil and the resulting diffraction pattern in the image. In panel (*a*), one can count approximately 10 cycles of the sinusoid across the entire pupil. In the image (*b*), this modulation of the DM creates a pair of speckles (pointed at by white arrows) located 10 λ/D away from the center of the field. These additional speckles interfere with the already present diffraction features such as rings, spikes, and phase defects. However, they do not interfere with incoherent structures like planets and disks.

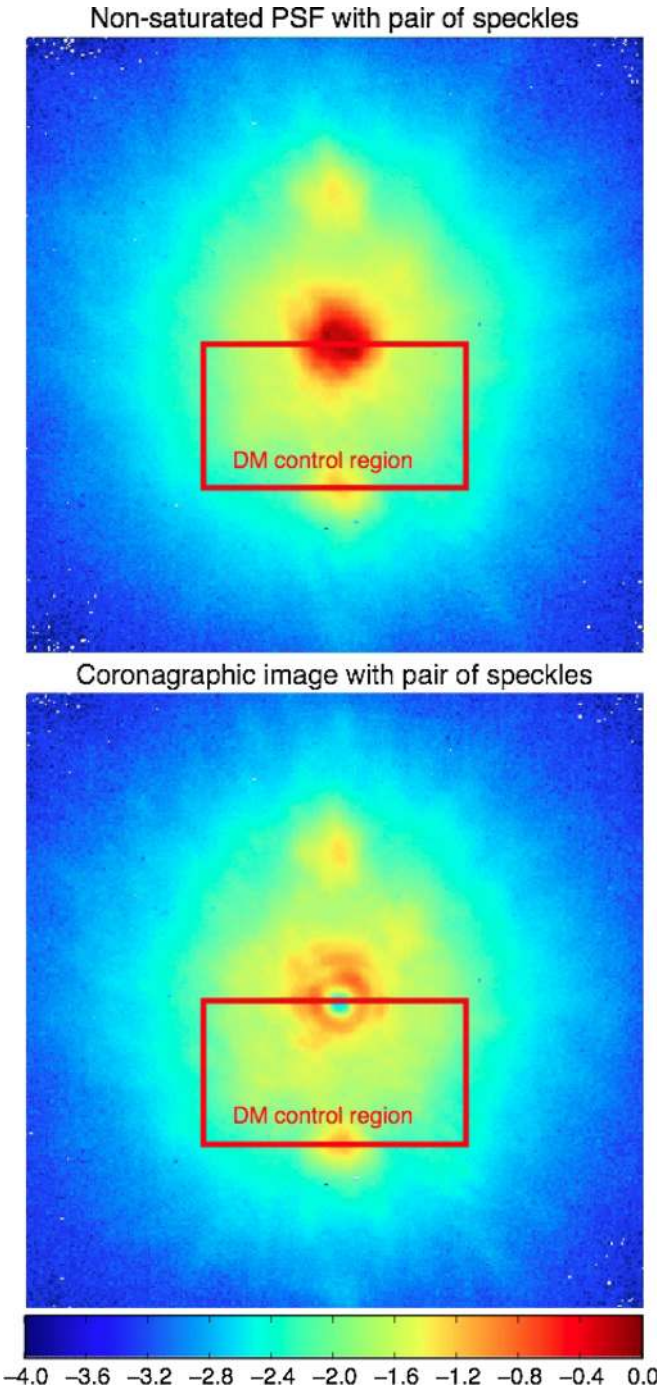

FIG. 3.—Comparison of a noncoronagraphic (*top panel*) and a coronagraphic (*bottom panel*) image acquired by HiCIAO behind SCExAO, with an added pair of speckles at max angular separation (log contrast scale). The red box highlights the area controlled by the DM during the experiments reported in this paper. Added speckles like these enable the calibration of the image in contrast, even if the central star is blocked by the coronagraph. See the electronic edition of the *PASP* for a color version of this figure.

4. ON-SKY SPECKLE NULLING

Martinache et al. (2012) showed, using SCExAO under stable laboratory conditions, that it is possible to actuate the DM before the PIAA coronagraph to create diffraction features that destructively interfere with speckles in the field, creating

a uniform high contrast region, often referred to as a "dark hole" in the image. Here, we apply the same iterative speckle nulling algorithm during actual on-sky observations. The major difference with the laboratory scenario is that the static (or quasi-static) features of the PSF probed by the speckle nulling algorithm are buried underneath a very strong, fast-varying dynamic component, due to the incomplete AO correction in the absence of a properly closed XAO loop.

The reported performance of ADI calibration suggests that high-contrast detection limits are set by long-lived aberrations, with a characteristic time-scale ∼1 hr or less. In this experiment, the science detector (HiCIAO) and the speckle-nulling camera cannot simultaneously observe: a retractable mirror sends the light either way. To be useful, the speckle nulling loop must therefore converge within a time-scale on the order of 15–20 minutes, so that sufficient time is left for the acquisition of frames by the (slow) science detector, before the quasi-static aberrations start changing again.

4.1. Technical Constraints

This on-sky speckle nulling experiment was performed using an uncooled InAsGa type detector (Xeva XS 1.7-320, sold by Xenics), and an H-broadband filter (1.6 μm). Such cameras exhibit frame rates up to ∼100 Hz that make them appealing for NIR wavefront control applications; however, they also have fairly high readout noise (>300 e^-) as well as high dark current. In the high-gain setting, the dark current averages 10000 counts in 20 ms exposure (almost the entire usable dynamic range). Coronagraphic observations with these cameras are therefore limited to very bright stars only.

The images showed here were obtained while observing the bright K-type star Pollux ($V = 1.15$, $R = 0.6$, $H = -0.845$). For this object, the best compromise was to use a 10-ms exposure time in low-gain mode, with a median dark current level ∼4200. While the speckle nulling loop is running, the camera continuously acquires 10-ms exposures at the frame rate of 30 Hz.

In a given image, up to n speckles are identified within the control region and their positions marked, relative to the central source, hidden by the coronagraph, but nevertheless located by the satellite speckles as described in section 3. The first step is to identify the two-component spatial frequency (k_x, k_y) of the DM that corresponds to each of the speckles identified inside the control region (cf. Fig. 2). The amplitude α_0 of this spatial frequency is estimated from the speckle brightness, proportional to the square of the amplitude α_0. The only remaining unknown is the phase φ of the speckle, which can take any value between 0 and 2π.

To determine this unknown, one modulates the DM with a sinusoidal function so as to generate a speckle probe of constant amplitude α_0, but whose phase is varied from 0 to 2π radians from image-to-image. By tracking the evolution of the resulting speckle brightness as a function of the probe phase, one is able to determine the true phase φ_0 of the original speckle. Once the speckle phase is determined, a correction of opposite phase $\varphi_0 + \pi$ and of amplitude $g \times a_0$ (with $g \sim 0.1$ the loop gain), is permanently applied before the loop is allowed to hunt for other speckles. A minimum of four probes with phase 0, $\pi/2$, π, and $3\pi/2$ is required to unambiguously estimate a long-lived quasi-static speckle phase. Unfortunately, the 10-ms exposure time imposed by the characteristics of the detector happens to be of the order of the time scale of the AO188 wavefront correction. To make the speckle nulling loop robust against fast fluctuations associated to the dynamic speckle component, the algorithm uses 30 probes of phase uniformly varying between 0 and 2π.

After the speckle nulling loop has converged, a mirror located in a collimated beam after the coronagraph (cf. Fig. 1) is translated out of the optical path so as to direct the light toward the HiCIAO imager.

Given the chosen number of probes, frame rate, and processing time, we get one iteration completed in 4 s. We increase the efficiency of the loop by simultaneously probing as many speckles as possible. However, the image-to-image variance due to the dynamic aberrations and the poor sensitivity of the camera set a limit to the total number of speckles that can be probed. In practice, the algorithm tested on-sky was able to simultaneously probe an average of five of the brightest speckles in the field.

4.2. Speckle Nulling Data

Twelve minutes of the speckle nulling loop running were sufficient to allow us to visually observe a darkening of one side of the field of view. To test the efficiency of the wavefront modulation resulting from the speckle nulling loop, several series of images were acquired with HiCIAO, alternating between a "flat" and an "optimized" SCExAO DM shape. The flat DM shape resulted from an optimization routine maximizing the Strehl in the noncoronagraphic image using Zernike modes: astigmatism, focus, coma, spherical, trefoil, and quadrifoil on an internal calibration source. The optimized shape was the result of speckle nulling corrections applied in addition to the flat. The complete acquisition sequence consisted of four such cycles (to make the analysis robust against slow trend effects), resulting in a total of twenty 5-second exposure frames per DM shape. These HiCIAO images were dark-subtracted and flat-fielded, using standard data reduction procedures established for the reduction of the SEEDS data, assembled into two data cubes.

The images gathered in Figure 4 summarize the statistical properties of these two datacubes, looking at the median (*left column*) and the standard deviation (*right column*) for the flat (*top row*) as well as the optimized (*bottom row*) DM shape, using common colorbars. For each figure, the extent of the control region is highlighted by a red box, which, for this experiment, is located in the lower part of the HiCIAO image.

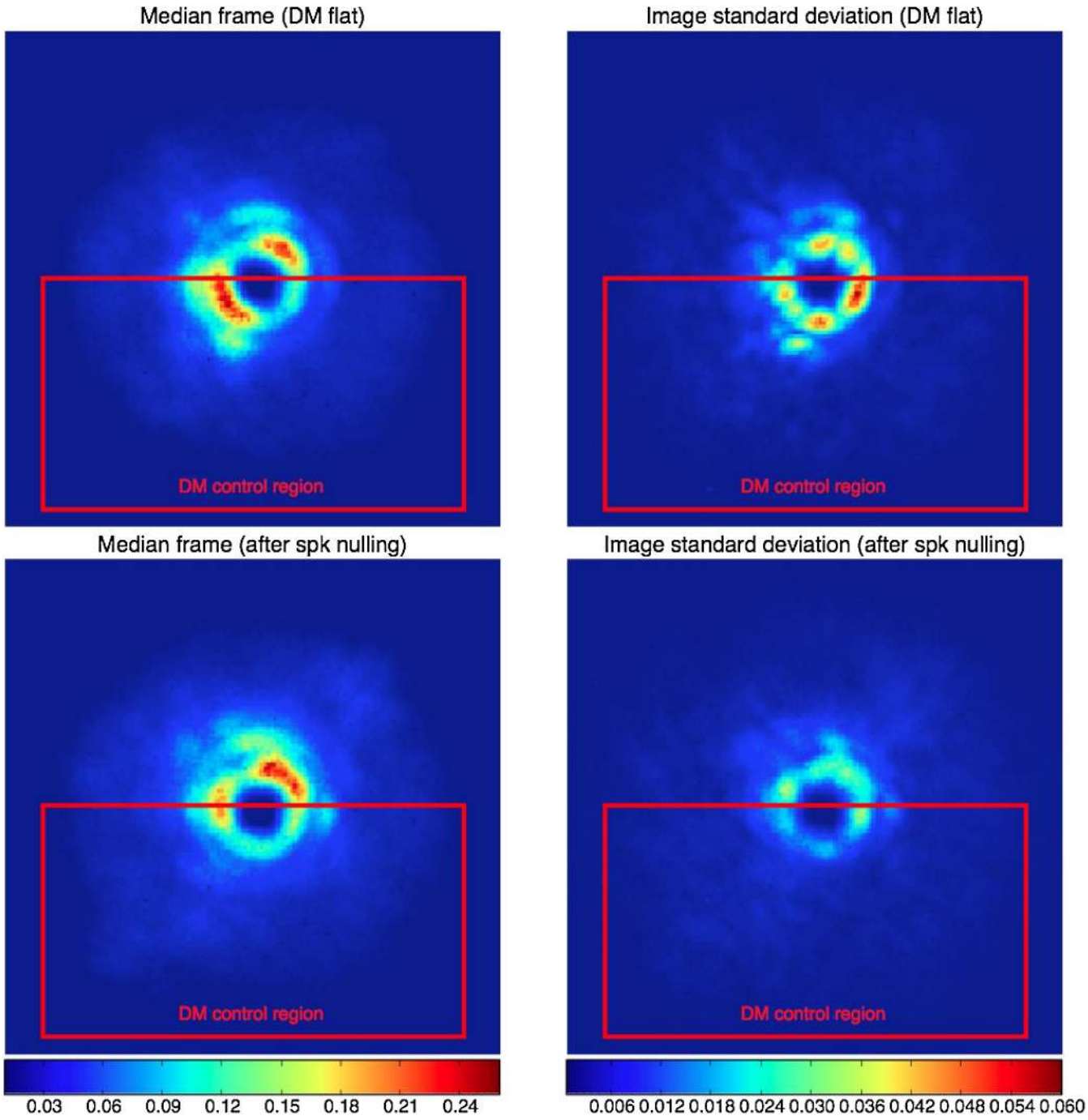

FIG. 4.—Statistical properties (median and standard deviation) of coronagraphic images acquired by HiCIAO for two SCExAO DM shapes. The top row is for a flat DM shape that maximizes the Strehl ratio. The bottom row is for a DM shape resulting from a speckle nulling loop. The colorbar scale used for the images on the left (median) is calibrated in contrast. See the electronic edition of the *PASP* for a color version of this figure.

The combination of exposure time (5 s) and neutral density (ND0.1) for HiCIAO was chosen to acquire nonsaturated images in the H-broadband filter. The low and fast varying seeing experienced during the acquisition and the lack of a yet to come high-order close-loop adaptive correction results in exposures that exhibit no obvious individual speckles in the field, a major difference from what is already achieved by XAO equiped instruments (see, e.g., Fig. 1 of Oppenheimer et al. [2013]). The first bright ring, located at a radius of 2.3 λ/D, is the dominating feature in the images. Note that this radius is very close to the quoted IWA of SCExAO (2.2 λ/D), defined as the angular separation for which the coronagraph throughput reaches 50%

(Martinache et al. 2012), and imposed by the focal plane mask. The standard deviation of the DM flat datacube shows that most of the speckle variance is localised onto the diffraction rings.

The speckle nulling algorithm unsurprisingly focused its efforts onto this area of the image. With the optimized DM shape (bottom images in Fig. 4), the median flux for the part of the diffraction ring overlapping with the control region is reduced. The improvement in regards to the median is moderate as the brightest parts of the ring are attenuated by a factor of 2.

4.3. Benefit for High Contrast Imaging

The detection of faint structures in a speckle-noise dominated problem is usually achieved by some form of PSF subtraction. The PSF can be obtained from more or less sophisticated methods: from the direct observation of a reference star to a synthetic PSF obtained after ADI. PSF subtraction is obviously appropriate to calibrate static features of the PSF. It is also good for fast-varying speckles that average down quickly to a smooth halo.

However, PSF subtraction fails to calibrate speckles characterized by a timescale of a few minutes which manifest by residual variance in PSF subtracted images: the speckle noise. The top row of Figure 4 illustrates this phenomenon and shows that, over the course of the twelve minutes covered by the experiment, on the most prominent image features the fluctuations are on the order of 25–50% of the local median value, and that the overall structure of the standard deviation image follows that of the median; static aberrations do appear to mix with and amplify the local speckle noise, resulting in speckles pinned on the static diffraction pattern (Aime & Soummer 2004).

In actively suppressing the static features of the coronagraphic PSF (cf. bottom row of Fig. 4), speckle nulling achieves two goals: it removes slow and static speckles (measurable by comparing the flat and optimized median frames) and reduces the speckle noise (measurable by comparing the standard deviation frames). The PSF mean level over the region corrected by speckle nulling is not only lower by a factor of 2, it is also more stable, with a standard deviation reduced by a factor of 3.

5. CONCLUSION

This paper presents the first demonstration of speckle nulling performed on-sky with partial AO correction. In the context of the SCExAO project, using a PIAA coronagraph and a deformable mirror to modulate the focal plane, the results presented here show that it is indeed possible to complement ADI and its variants at small angular separations, even in the absence of a high strehl AO system, and therefore in the presence of a brighter dynamic speckle halo.

Speckle nulling offers improvement at two levels: (1) it removes slow speckles, resulting in images with enhanced contrast before processing, and (2) it reduces the speckle noise amplification by the static diffraction, resulting in enhanced post-processing detection limits. Moreover, it enables this in a regime of angular separation that cannot be addressed by ADI, which remains the reference technique (Brandt et al. 2013) for the calibration of ground based AO PSF. In spite of unfavorable observing conditions, the control loop managed to remain stable and converged to improve the statistical properties of the coronagraphic image.

While consistent, the reported improvement remains modest, and this can in part be attributed to the choices of integration time, constrained by the noise properties of the detector used during the speckle nulling loop. Improving the sensitivity and the dynamical range of the image by using a cooled detector will increase the flexibility of the technique and allow a more efficient use of the observing time. The real performance improvement, however, will come from the use of an actual close-loop XAO system that will improve the raw Strehl of individual images.

Advanced focal plane based wavefront techniques such as electric field conjugation (Give'On 2006; Bordé & Traub 2006) have been used extensively on laboratory high contrast test-beds over the world, including with a PIAA coronagraph like the one used on SCExAO (Guyon et al. 2010) providing access to very high contrast (10^{-7} and beyond) detection limits in a stable environment. The fact that, even in difficult observing conditions, a speckle nulling driven wavefront control algorithm originally envisioned for stable test-benches remains operational is very encouraging. This indeed suggests that, with only a few adaptations, all of the high contrast laboratory work that has so far been geared toward space borne applications is relevant to ground based observations, even with partial AO correction.

REFERENCES

Aime, C., & Soummer, R. 2004, ApJ, 612, L 85

Bordé, P. J., & Traub, W. A. 2006, ApJ, 638, 488

Brandt, T. D., McElwain, M. W., Turner, E. L., Abe, L., Brandner, W., Carson, J., Egner, S., Feldt, M., et al. 2013, ApJ, 764, 183

Clergeon, C., Guyon, O., Martinache, F., Veran, J., Correia, C., Garrel, V., & Jovanovic, N. 2013, American Astronomical Society Meeting Abstracts, 221

Give'On, A. 2006, PhD thesis, Princeton University

Guyon, O. 2003, A&A, 404, 379

Guyon, O., Matsuo, T., & Angel, R. 2009, ApJ, 693, 75

Guyon, O., Pluzhnik, E. A., Galicher, R., Martinache, F., Ridgway, S. T., & Woodruff, R. A. 2005, ApJ, 622, 744

Guyon, O., Pluzhnik, E., Martinache, F., Totems, J., Tanaka, S., Matsuo, T., Blain, C., & Belikov, R. 2010, PASP, 122, 71

Hinkley, S., Pueyo, L., Faherty, J. K., Oppenheimer, B. R., Mamajek, E. E., Kraus, A. L., Rice, E. L., Ireland, M. J., et al. 2013, ApJ, 779, 153

Hodapp, K. W., Suzuki, R., Tamura, M., Abe, L., Suto, H., Kandori, R., Morino, J., Nishimura, T., et al. 2008, Proc. SPIE, 7014
Ireland, M. J. 2013, MNRAS, 433, 1718
Lafrenière, D., Marois, C., Doyon, R., Nadeau, D., & Artigau, É. 2007, ApJ, 660, 770
Macintosh, B. A., Graham, J. R., Palmer, D. W., Doyon, R., Dunn, J., Gavel, D. T., Larkin, J., Oppenheimer, B., et al. 2008, Proc. SPIE, 7015
Marois, C., Lafrenière, D., Doyon, R., Macintosh, B., & Nadeau, D. 2006, ApJ, 641, 556
Martinache, F. 2010, ApJ, 724, 464
Martinache, F., Guyon, O., Clergeon, C., & Blain, C. 2012, PASP, 124, 1288
Martinache, F., Guyon, O., Garrel, V., Clergeon, C., Groff, T., Stewart, P., Russell, R., & Blain, C. 2011, Proc. SPIE, 8151
Mawet, D., Serabyn, E., Liewer, K., Burruss, R., Hickey, J., & Shemo, D. 2010, ApJ, 709, 53
Minowa, Y., Hayano, Y., Oya, S., Watanabe, M., Hattori, M., Guyon, O., Egner, S., Saito, Y., et al. 2010, Proc. SPIE, 7736
Oppenheimer, B. R., Baranec, C., Beichman, C., Brenner, D., Burruss, R., Cady, E., Crepp, J. R., Dekany, R., et al. 2013, ApJ, 768, 24
Oppenheimer, B. R., Beichman, C., Brenner, D., Burruss, R., Cady, E., Crepp, J., Hillenbrand, L., Hinkley, S., et al. 2012, Proc. SPIE, 8447
Pope, B., Martinache, F., & Tuthill, P. 2013, ApJ, 767, 110
Sauvage, J.-F., Fusco, T., Petit, C., Meimon, S., Fedrigo, E., Suarez Valles, M., Kasper, M., Hubin, N., et al. 2010, Proc. SPIE, 7736
Sivaramakrishnan, A., & Oppenheimer, B. R. 2006, ApJ, 647, 620
Tamura, M. 2009, in AIP Conf. Proc. 1158, Exoplanets and Disks: Their Formation and Diversity, ed. T. Usuda, M. Tamura, & M. Ishii (New York: AIP), 11–16
Tuthill, P., Lloyd, J., Ireland, M., Martinache, F., Monnier, J., Woodruff, H., ten Brummelaar, T., Turner, N., et al. 2006, Proc. SPIE, 6272
Vogt, F. P. A., Martinache, F., Guyon, O., Yoshikawa, T., Yokochi, K., Garrel, V., & Matsuo, T. 2011, PASP, 123, 1434